



## Two-Phase Modeling and Flooding Prediction of Polymer Electrolyte Fuel Cells

Ugur Pasaogullari\* and Chao-Yang Wang\*\*<sup>z</sup>

Electrochemical Engine Center and Department of Mechanical and Nuclear Engineering, The Pennsylvania State University, University Park, Pennsylvania 16802, USA

A newly developed theory of liquid water transport in hydrophobic gas diffusion layers is applied to simulate flooding in polymer electrolyte fuel cells (PEFCs) and its effects on performance. The numerical model accounts for simultaneous two-phase flow and transport of species and electrochemical kinetics, utilizing the well-established multiphase mixture formulation to efficiently model the two-phase transport processes. The two-phase model is developed in a single domain, yielding a single set of governing equations valid in all components of a PEFC. The model is used to explore the two-phase flow physics in the cathode gas diffusion layer. Multidimensional simulations reveal that flooding of the porous cathode reduces the rate of oxygen transport to the cathode catalyst layer and causes a substantial increase in cathode polarization. Furthermore, the humidification level and flow rate of reactant streams are key parameters controlling PEFC performance and two-phase flow and transport characteristics. It is also found that minimization of performance limitations such as membrane dry-out and electrode flooding depends not only on material characteristics but also on the optimization of these operating parameters.

© 2005 The Electrochemical Society. [DOI: 10.1149/1.1850339] All rights reserved.

Manuscript submitted May 19, 2004; revised manuscript received July 23, 2004. Available electronically January 11, 2005.

Water management in polymer electrolyte fuel cells (PEFCs) generally involves balancing the operation to avoid flooding while maintaining membrane hydration. This is critical for achieving the highest possible performance.<sup>1-8</sup> The currently utilized polymer electrolyte membranes must be fully hydrated to exhibit high proton conductivity. However, when too much water accumulates in the cathode, it condenses and blocks some of the open pores, reducing the available path for oxygen transport, resulting in a phenomenon commonly called "flooding." Although flooding is generally associated with the higher current densities due to the larger water production, it is also commonly observed even at low current densities, particularly under low gas flow rates and lower operating temperatures. It is clear that two-phase transport of reactants and products constitutes a limiting factor of PEFC performance, and the understanding of the gas-liquid two-phase transport is of great importance for PEFC operation. Operating conditions and membrane electrode assembly (MEA) components have to be well characterized to achieve optimal performance. In this respect, a comprehensive numerical model is a useful tool for understanding and describing the two-phase processes that occur during PEFC operation.

Many models of various complexities have been presented by several research groups for predicting PEFC performance. Early contributions include the one-dimensional studies of Bernardi and Verbrugge<sup>9-11</sup> and Springer *et al.*<sup>12,13</sup>. Gurau *et al.*<sup>14</sup> became the first to analyze the two-dimensional effects on PEFC operation in the single-phase transport conditions. Um *et al.*<sup>15</sup> have presented a computational fluid dynamics (CFD) based single-phase multidimensional PEFC model based on the electrochemical modeling framework by Wang *et al.*<sup>16</sup> The above-mentioned studies introduced some fundamental knowledge on internal characteristics of PEFC operation and laid the foundation of PEFC modeling; however, none of them analyzed the two-phase transport in PEFCs. Some modeling studies considered the effect of flooding on performance without attempting to analyze the transport of liquid water by a given flooding parameter.<sup>12,13,17</sup> He *et al.*<sup>18</sup> have proposed a two-dimensional, two-phase model for PEFC with interdigitated flow field, in which they included capillary transport of liquid water in a completely wetted (*i.e.*, hydrophilic) gas diffusion layer (GDL). Based on this model, two-phase transport in PEFCs with conventional gas channels is also analyzed.<sup>19</sup> Wang *et al.*<sup>20</sup> have developed a two-phase model of the air cathode of PEFC, which is based on the multiphase mixture ( $M^2$ ) formulation by Wang and Cheng<sup>21</sup> also with a hydro-

philic GDL. Subsequently, You and Liu<sup>22</sup> published a similar work investigating the effects of several operating parameters on two-phase transport. Most recently, Mazumder and Cole<sup>23</sup> presented a numerical study, also based on the  $M^2$  model of Wang and Cheng;<sup>21</sup> however, their model appears to be valid only in the two-phase regime where there is liquid water. Under low-humidity inlet conditions where the liquid saturation is zero, the model of Mazumder and Cole yielded zero electro-osmotic drag through the polymer membrane. Berning and Djilali<sup>24</sup> also presented a two-phase model for a porous GDL and gas channel of a PEFC while excluding the MEA. Water transport through the MEA is thus completely ignored. Berning and Djilali also failed to address the effect of the GDL hydrophobic property. None of these above-mentioned studies are intended to investigate and analyze two-phase transport in hydrophobic GDL. A brief review of this subject was given by Wang.<sup>25</sup>

The theory of liquid water transport in a hydrophobic GDL remained unclear until recently. Nam and Kaviani<sup>26</sup> developed a one-dimensional model describing the liquid water transport through hydrophobic GDL. In this model, the gas phase pressure is assumed to be uniform, thereby rendering the liquid phase transport governed by only the gradient in capillary pressure. The model was used to assess the effects of GDL fiber diameter, porosity, and capillary pressure on the liquid water distribution. Independently, based on extensive experimental observations of liquid water flow in an operating PEFC, Pasaogullari and Wang<sup>27</sup> most recently proposed a systematic theory of liquid water transport through hydrophobic GDL.

The objective of the present study is to present a predictive capability for flooding in multidimensional, full PEFC with realistic hydrophobic GDL based on the theory presented in Ref. 27. In addition, it is of interest to investigate the effects of operating conditions, such as inlet humidification and flow rates, on the two-phase transport and performance of PEFC.

In the next section, a two-phase, multidimensional PEFC model is described. A comparison of single- and two-phase model predictions is given, and the effects of two-phase transport and flooding on PEFC performance are discussed, along with a detailed discussion of the effects of the flow rate, *i.e.*, the flow stoichiometry and the inlet humidity. Major conclusions are summarized in the last section, and future work based on the present modeling framework is identified.

### Numerical Model

Traditionally, macroscopic problems of two-phase flow and transport in porous media have been modeled using a two-fluid approach. However, this approach results in a large number of primary variables for each phase, and highly nonlinear equations. Therefore,

\* Electrochemical Society Student Member.

\*\* Electrochemical Society Active Member.

<sup>z</sup> E-mail: cxw31@psu.edu

**Table I. A two-phase PEFC model: Governing equations with source/sink terms in catalyst layers.**

	Conservation equation	Source terms
Mass	$\frac{\partial(\rho\varepsilon)}{\partial t} + \nabla \cdot (\rho\mathbf{u}) = 0$	
Momentum	$\frac{1}{\varepsilon} \left[ \frac{\partial(\rho\mathbf{u})}{\partial t} + \frac{1}{\varepsilon} \nabla \cdot (\rho\mathbf{u}\mathbf{u}) \right] = \nabla \cdot (\mu^{\text{eff}}\nabla\mathbf{u}) - \nabla p + \rho_k\mathbf{g} - \frac{\mu^{\text{eff}}}{K}\mathbf{u}$	$S^i = \frac{S^k}{nF}j$
Species	$\frac{\partial(C^i)}{\partial t} + \nabla \cdot (\gamma_c\mathbf{u}C^i) = \nabla \cdot [D_g^{i,\text{eff}}\nabla C_g^i] - \nabla \cdot \left[ \left( \frac{mf_1^i}{M^i} - \frac{C_g^i}{\rho_g} \right) \mathbf{j}_i \right] - \nabla \cdot \left( \frac{n_d}{F} i_c \right) + S^i$	
Charge	$\nabla \cdot (\kappa_c^{\text{eff}}\nabla\Phi_e) + S_\Phi = 0$	$S_\Phi = j$

Electrochemical reaction:

$$\sum s_k M_k = ne^- \quad \text{where} \quad \begin{cases} M_k: \text{chemical formula of species } k \\ s_k: \text{stoichiometry coefficient} \\ n: \text{number of electrons transferred} \end{cases}$$

In PEFCs, there are:

Anode hydrogen oxidation reaction (HOR)  $\text{H}_2 - 2\text{H}^+ \rightarrow 2e^-$

Cathode oxygen reduction reaction (ORR)  $2\text{H}_2\text{O} - \text{O}_2 - 4\text{H}^+ \rightarrow 4e^-$

exact solutions of two-phase problems with two-fluid models are limited to a very limited number of problems with many simplifying assumptions. Furthermore, the two-fluid models require explicitly tracking the irregular and moving interface between two phases, increasing the numerical complexity of the problem.<sup>28</sup> Particularly in PEFCs, the gas-liquid interfaces, *i.e.*, the condensation and evaporation fronts, are expected as well as the coexistence of single- and two-phase regions. Therefore, a convenient model capable of describing both single- and two-phase regions without a need to track the irregular, *a priori* unknown interface is required. For these reasons, the multiphase mixture ( $M^2$ ) formulation of Wang and Cheng<sup>21</sup> is particularly suitable for two-phase PEFC modeling. The  $M^2$  model is a mathematical reformulation of the classical two-phase model that views the multiphase system as a chemical mixture. With this approach, the multiphase flow is then described in terms of a mass-averaged mixture velocity and diffusive flux, representing the difference between the mixture velocity and individual phase velocity. One major advantage of the  $M^2$  model over the classical two-fluid models is that it eliminates the need for tracking phase interfaces, thus simplifying the numerical complexity of two-phase flow and transport modeling. Another salient feature of the  $M^2$  model for PEFC is that all model equations are valid in all three types of regions possible in a PEFC: single-phase gas, liquid-gas two-phase, and single-phase liquid. Finally, the  $M^2$  model is mathematically equivalent to two-fluid models without invoking any additional approximations. These aforementioned advantages render the  $M^2$  model to be a suitable and widely adopted two-phase flow and transport modeling framework for PEFCs.<sup>20,22,23</sup>

**Model assumptions.**—Utilizing the  $M^2$  formulation for two-phase transport, the proposed model incorporates the following assumptions: (i) incompressible gas mixtures, (ii) laminar flow due to a Reynolds number of the order of several hundreds, (iii) isothermal cell condition, (iv) isotropic and homogeneous porous GDL, characterized by an effective porosity and a permeability, and (v) negligible potential drop due to ohmic resistance in the electronically conductive solid matrix of GDL and catalyst layers, as well as bipolar plates. Furthermore, two-phase mist flow (*i.e.*, homogeneous flow) is assumed to be present inside the gas channels. Therefore, the gas and liquid phase velocities are equal to each other in the gas channel, resulting in a very small fraction of liquid water in the gas stream in the gas channel. Consequently, the coverage of GDL surface by liquid droplets becomes very small, and is neglected in this work.

**Governing equations.**—With the preceding assumptions, PEFC

operation is governed by conservation of mass, momentum, species, and charge. A single-domain formulation is used for the governing equations, which are valid for an entire PEFC, eliminating the requirement of interfacial conditions between the components. Table I lists the governing equations with their corresponding source/sink terms in the catalyst layers due to the electrochemical reactions. Note that, in the present model, superficial velocities are used for the porous zones to automatically satisfy the mass continuity at the open channel-porous media interface (*e.g.*, GDL-channel interface). Here, the two-phase mixture viscosity and density is given by<sup>21</sup>

$$\mu = \frac{\rho_l \cdot s + \rho_g \cdot (1 - s)}{\frac{k_{rl}}{\nu_l} + \frac{k_{rg}}{\nu_g}} \quad [1]$$

$$\rho = \rho_l \cdot s + \rho_g \cdot (1 - s) \quad [2]$$

Here,  $s$  and  $(1 - s)$  denote the volume fraction of the open pore space occupied by the liquid and gas phases, respectively. The momentum equation is modified to be valid both in the porous medium and the open channel, reducing to the two-phase Darcy's law within the porous medium with a small permeability. Inside the flow channel, porosity and permeability are equal to unity and infinity, respectively. Because the available pore space in the porous GDL is shared by gas and liquid phases, a relative permeability concept is introduced. The relative permeability,  $k_{rk}$ , represents the ratio of intrinsic permeability of phase  $k$  at a given saturation level,  $s$ , to the total intrinsic permeability of the porous GDL. In this work, we assume that the relative permeabilities of individual phases are relative to the cube of phase saturations, *i.e.*

$$k_{rl} = s^3 \quad k_{rg} = (1 - s)^3 \quad [3]$$

The species conservation equation presented in Table I is written in molar concentration, instead of the original form in mass fraction provided in Ref. 21, and a derivation of the current form is provided in the Appendix. Here, we define the molar concentration as the total molar concentration in both the liquid and gas phases. That is

$$C^i M^i = \rho m f^i \quad [4]$$

The second term on the left-hand side of the species equation in Table I represents the advective term, in which the advection correction factor,  $\gamma_c$ , is given by

$$\gamma_c = \begin{cases} \frac{\rho}{C^{\text{H}_2\text{O}}} \left( \frac{\lambda_1}{M^{\text{H}_2\text{O}}} + \lambda_g \frac{C^{\text{H}_2\text{O}}_{\text{sat}}}{\rho_g} \right) & \text{for water} \\ \frac{\rho \lambda_g}{\rho_g(1-s)} & \text{for other species} \end{cases} \quad [5]$$

where the relative mobilities of individual phases,  $\lambda_k$ , are

$$\lambda_1(s) = \frac{k_{n1}/v_1}{k_{n1}/v_1 + k_{rg}/v_g} \quad \lambda_g(s) = 1 - \lambda_1(s) \quad [6]$$

Note that the two-phase species equation listed in Table I reduces to its counterparts of single-gas and single-liquid species equations at liquid saturations approaching 0 and unity, respectively.

The last three terms of the species conservation equation in Table I represent the capillary transport, electro-osmotic drag of water in the membrane, and source/sink terms due to electrochemical reactions, respectively. The theory of capillary transport in hydrophobic GDL has been described in detail by Pasaogullari and Wang.<sup>27</sup> The capillary flux,  $\mathbf{j}_l$ , is<sup>21</sup>

$$\mathbf{j}_l = \frac{\lambda_l \lambda_g}{\nu} K [\nabla p_c + (\rho_l - \rho_g) \mathbf{g}] \quad [7]$$

where  $p_c$  is the capillary pressure and is given by<sup>21</sup>

$$p_c = \sigma \cos(\theta_c) \left( \frac{\varepsilon}{K} \right)^{1/2} J(s) \quad [8]$$

Here,  $J(s)$  is the Leverett function, and it is given for both hydrophobic and hydrophilic GDL as<sup>26,27</sup>

$$J(s) = \begin{cases} 1.417(1-s) - 2.120(1-s)^2 + 1.263(1-s)^3 & \text{if } \theta_c < 90^\circ \\ 1.417s - 2.120s^2 + 1.263s^3 & \text{if } \theta_c > 90^\circ \end{cases} \quad [9]$$

Although the Leverett function is used for its functional form between  $p_c$  and  $s$ , its precise expression requires experimental calibration of various GDLs.

Note that the gas phase diffusion coefficient is an effective one, modified via the Bruggeman correlation<sup>29</sup> to account for the effects of porosity and tortuosity of porous electrodes and catalyst layers. Furthermore, in the two-phase zone, the gas phase is saturated with water vapor and, because the cell is isothermal, the water concentration in the gas phase is uniform; hence, the gas phase diffusion of water vanishes. Therefore, the gas phase diffusion coefficient is

$$D_g^{\text{i,eff}} = [\varepsilon(1-s)]^{1.5} D_g^{\text{i}} \quad \text{for species other than H}_2\text{O} \\ D_g^{\text{H}_2\text{O,eff}} = \varepsilon^{1.5} D_g^{\text{H}_2\text{O}} \quad \text{when } s = 0 \quad (\text{i.e., } C^{\text{H}_2\text{O}} \leq C^{\text{H}_2\text{O}}_{\text{sat}}) \quad [10]$$

$$D_g^{\text{H}_2\text{O,eff}} = 0 \quad \text{when } s > 0 \quad (\text{i.e., } C^{\text{H}_2\text{O}} > C^{\text{H}_2\text{O}}_{\text{sat}})$$

*Transport properties of electrolyte.*—The species conservation equation reduces to the following form for water species in the membrane<sup>30</sup>

$$\frac{\partial(C^{\text{H}_2\text{O}})}{\partial t} = \nabla \cdot (D^{\text{H}_2\text{O,eff}} \nabla C^{\text{H}_2\text{O}}) - \nabla \cdot \left( n_d \frac{I_e}{F} \right) \quad [11]$$

Note that permeation of liquid water due to the hydraulic pressure gradient across the membrane has been neglected in Eq. 11 due to the small pressure gradients and hydraulic permeability of the membrane (i.e., on the order of  $10^{-19} \text{ m}^2$ ).<sup>10</sup>

In this work, we define

$$a = \frac{C^{\text{H}_2\text{O}}}{C^{\text{H}_2\text{O}}_{\text{sat}}} \quad [12]$$

It is clear that  $a$  is the water activity in the pure gas region and approaches unity when the gas becomes saturated with water vapor. However, in the two-phase zone,  $a$  is greater than unity and linearly proportional to the liquid saturation, as shown below

$$a = \frac{\frac{\rho_l}{M^{\text{H}_2\text{O}}} s + C^{\text{H}_2\text{O}}_{\text{sat}}(1-s)}{C^{\text{H}_2\text{O}}_{\text{sat}}} = (1-s) + \frac{\rho_l}{M^{\text{H}_2\text{O}} C^{\text{H}_2\text{O}}_{\text{sat}}} s \quad [13]$$

We then extrapolate the membrane water uptake curve for all values of  $a$  as follows

$$\lambda = \begin{cases} 0.043 + 17.18a - 39.85a^2 + 36.0a^3 & \text{for } 0 \leq a \leq 1 \\ 14 + 14(a-1) & \text{for } 1 \leq a \leq 3 \\ 16.8 & \text{for } a > 3 \end{cases} \quad [14]$$

The first part of this correlation was fitted by Springer *et al.*<sup>12</sup> to the experimental data of the polymer membrane in equilibrium with gas. The second portion is an extrapolation also made in Ref. 12 to cover the range of the membrane in equilibrium with a two-phase mixture having small liquid saturation, i.e.,  $1 < a < 3$ . When  $a > 3$  (i.e., a more significant two-phase region), the membrane is assumed to be fully saturated with liquid water, and thus having the water content  $\lambda$  equal to 16.8.

We use the following correlations of the electro-osmotic drag coefficient,  $n_d$ , the water diffusivity,  $D^{\text{H}_2\text{O}}_{\text{mem}}$ , and the proton conductivity,  $\kappa_e$ <sup>12,31</sup>

$$n_d = \frac{2.5\lambda}{22} \quad [15]$$

$$D_e^{\text{H}_2\text{O}} = \begin{cases} 3.1 \times 10^{-7} \lambda (e^{0.28\lambda} - 1) e^{-2346/T} & \text{for } 0 < \lambda \leq 3 \\ 4.17 \times 10^{-8} \lambda (1 + 161 \cdot e^{-\lambda}) e^{-2346/T} & \text{for } \lambda > 3 \end{cases} \quad [16]$$

$$\kappa_e = (0.5139\lambda - 0.326) \exp \left[ 1268 \left( \frac{1}{303} - \frac{1}{T_{\text{cell}}} \right) \right] \quad [17]$$

Again using the Bruggeman correlation, the proton conductivity of the catalyst layers is given by

$$\kappa_e^{\text{eff}} = \varepsilon_{\text{mc}}^{1.5} \kappa_e \quad [18]$$

where  $\varepsilon_{\text{mc}}$  is the fraction of the membrane phase in the catalyst layer.

*Electrochemical kinetics.*—The source term in the charge equation represents the transfer current between the electronically conductive solid matrix and the electrolyte phase in each of the anode and cathode catalyst layers. In PEFC, the anode HOR exhibits facile electrokinetics and hence a low surface overpotential; therefore, it can be expressed by a linear kinetic rate equation, whereas the cath-

ode ORR has relatively slow kinetics with higher surface overpotential, so that it can be adequately described by Tafel kinetics, *i.e.*

$$j_a = a i_{0,a}^{\text{ref}} \left( \frac{C_{\text{H}_2}}{C_{\text{ref}}^{\text{H}_2}} \right)^{1/2} \frac{\alpha_a + \alpha_c}{RT} F \eta \quad [19]$$

$$j_c = a i_{0,c}^{\text{ref}} \frac{C_{\text{O}_2}}{C_{\text{ref}}^{\text{O}_2}} \exp \left( -\frac{\alpha_c}{RT} F \eta \right) \quad [20]$$

where the sum of the transfer coefficients,  $\alpha_a + \alpha_c$ , is taken to be 2 for HOR and  $\alpha_c$  is set to 1 for ORR. The surface overpotential in the preceding equations,  $\eta$ , is defined as

$$\eta = \Phi_s - \Phi_e - U_o \quad [21]$$

where  $\Phi_s$  and  $\Phi_e$  denote the potentials of the electronic and electrolyte phases, respectively. The thermodynamic equilibrium potential,  $U_{o_2}$ , is zero on the anode but a function of temperature at the cathode<sup>32</sup>

$$U_o^{\text{cathode}} = 1.23 - 0.9 \times 10^{-3} (T - 298.15) \quad [22]$$

where  $T$  is in kelvins (K) and  $U_o$  is in volts (V). Under the assumption of a perfectly conductive electronic phase of anode and cathode catalyst layers,  $\Phi_s$  becomes zero for the anode and is equal to the cell voltage for the cathode.

It is not exactly known how liquid water blocks the access of electrons, protons, and reactants to active reaction sites and hence reduces the oxygen reduction rate. In this work, a directly proportional reduction in the active reaction surface with the liquid saturation is assumed, similar to some earlier studies.<sup>18-20</sup> That is

$$a_i^{\text{ref}} = (1 - s) a_o i_o^{\text{ref}} \quad [23]$$

where  $a_o$  is the total catalyzed and hence electrochemically active surface area per unit of catalyst layer volume. It is a function of Pt loading in mg/cm<sup>2</sup> and the catalyst layer thickness.

**Boundary conditions.**—The complete set of governing equations of the mathematical model is given in Table I. Boundary conditions are only required at the external boundaries due to the single-domain formulation. Phase potential boundary conditions are prescribed as a no-flux condition everywhere. The no-flux condition also applies for flow and transport equations for all boundaries except for channel inlets and outlets. At the inlets, the species concentrations and inlet velocities are specified as follows

$$\mathbf{u}_{\text{in}}^{\text{anode}} \cdot \mathbf{n}_{\text{in}}^{\text{anode}} = U_{a,\text{in}}; \quad \mathbf{u}_{\text{in}}^{\text{cathode}} \cdot \mathbf{n}_{\text{in}}^{\text{cathode}} = U_{c,\text{in}} \quad [24]$$

where

$$U_{a,\text{in}} = \frac{I_{\text{ref}} A_{\text{rxn}}}{2FC_{\text{in}}^{\text{H}_2} A_{\text{in}}} \zeta_a; \quad U_{c,\text{in}} = \frac{I_{\text{ref}} A_{\text{rxn}}}{4FC_{\text{in}}^{\text{O}_2} A_{\text{in}}} \zeta_c \quad [25]$$

$$C_{\text{anode}}^{\text{H}_2} = C_{\text{anode,in}}^{\text{H}_2}; \quad C_{\text{cathode}}^{\text{O}_2} = C_{\text{cathode,in}}^{\text{O}_2}; \quad [26]$$

$$C_{\text{anode}}^{\text{H}_2\text{O}} = C_{\text{anode,in}}^{\text{H}_2\text{O}}; \quad C_{\text{cathode}}^{\text{H}_2\text{O}} = C_{\text{cathode,in}}^{\text{H}_2\text{O}}; \quad [27]$$

At the outlets, fully developed flow is assumed with given back pressure. No diffusive flux boundary condition is prescribed for species equations.

**Numerical procedure.**—A sketch of the computational domain is given in Fig. 1. The resulting set of equations was discretized using a finite-volume method<sup>33</sup> and solved within the commercially available CFD software, Fluent, by customizing via user-defined functions. The software utilizes the well-known SIMPLE algorithm, and an algebraic multigrid solver to efficiently solve the resulting set of discretized linear equations. For details of the SIMPLE algorithm, the reader is referred to Ref. 33. Stringent numerical tests were

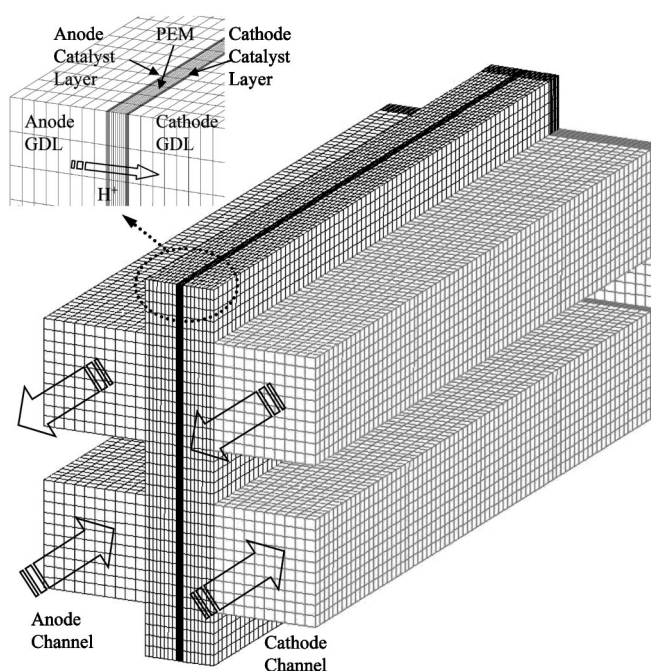


**Figure 1.** 3D two-channel serpentine flow-field cell geometry and computational mesh.

carried out to ensure that the solution was independent of the grid size. At least 10 computational volumes for every channel and current collector rib in the channel-channel (in-plane) direction, 6-8 computational volumes for every component of the MEA (*i.e.*, GDL, catalyst layer and membrane) in the anode to cathode direction (through plane), and 100-120 computational volume in the flow direction are required. For a single-channel three-dimensional (3D) flow field, this grid requirement results in approximately 100,000 computational cells, and the computation takes around 500 iterations in 5 h, with a 2 GHz PC.

Once the electrolyte phase potential field,  $\Phi_e$ , and the membrane conductivity are calculated, the local current density in the in-plane direction (*i.e.*, anode-to-cathode) is obtained by

$$I_e = -\kappa_e \cdot \frac{\partial \Phi_e}{\partial x} \quad [28]$$

and the average current density is

$$I_{\text{avg}} = \frac{1}{A_{\text{rxn}}} \int_{A_{\text{rxn}}} I_e \, dA \quad [29]$$

## Results and Discussion

**Comparison of single- and two-phase model predictions.**—To fully understand the effect of two-phase transport phenomena and flooding on PEFC operational characteristics, a detailed comparison between the single- and two-phase model predictions has been carried out for a 3D, two-channel serpentine flow-field PEFC geometry. The transport properties are listed in Table II, and the dimensions are given in Table III. The “single-phase model” uses the same governing equations of the two-phase model, but arbitrarily specifies a higher water saturation concentration so that water is assumed to be in a supersaturation state and does not condense into liquid; therefore the species transport and flow are treated as if they were gas phase only. Consequently, there is no liquid water present in the single phase model, and the effects of liquid water on electrochemical kinetics and species transport and flow are excluded. Presently, this single-phase approach is popularly exercised in the PEFC modeling field.

**Table II. Electrochemical and transport properties.**

Description	Value
Electrochemical kinetics (typical values)	
Anode reference exchange current density, $ai_{0,a}^{ref}$	$1.0 \times 10^9 \text{ A/m}^3$
Cathode reference exchange current density, $ai_{0,c}^{ref}$	$20,000 \text{ A/m}^3$
Anodic and cathodic transfer coefficients for HOR	$\alpha_a = \alpha_c = 1$
Cathodic transfer coefficient for ORR	$\alpha_c = 1$
Faraday constant, $F$	$96,487 \text{ C/mol}$
Universal gas constant, $R$	$8.314 \text{ J/mol K}$
Transport parameters	
H <sub>2</sub> diffusivity at 353 K and 1.5 atm <sup>34</sup>	$5.457 \times 10^{-5} \text{ m}^2/\text{s}$
O <sub>2</sub> diffusivity at 353 K and 1.5 atm <sup>34</sup>	$1.806 \times 10^{-5} \text{ m}^2/\text{s}$
H <sub>2</sub> O diffusivity in anode at 353 K and 1.5 atm <sup>34</sup>	$5.457 \times 10^{-5} \text{ m}^2/\text{s}$
H <sub>2</sub> O diffusivity in cathode at 353 K and 1.5 atm <sup>34</sup>	$2.236 \times 10^{-5} \text{ m}^2/\text{s}$
Liquid water viscosity <sup>34</sup>	$3.56 \times 10^{-4} \text{ Pa s}$
Anode gas viscosity <sup>34</sup>	$1.101 \times 10^{-5} \text{ Pa s}$
Cathode gas viscosity <sup>34</sup>	$1.881 \times 10^{-5} \text{ Pa s}$
Material properties	
Anode/cathode GDL porosity, $\epsilon_{GDL}$	0.5
Anode/cathode GDL permeability, $K_{GDL}$	$6.875 \times 10^{-13} \text{ m}^2$
Surface tension, $\sigma^{34}$	$0.0625 \text{ N/m}$
Contact angle of GDL, $\theta_c$	$110^\circ$
Volume fraction of membrane in catalyst layer, $\epsilon_{mc}$	0.2
Equivalent weight of membrane (Nafion 112), $EW$	$1.1 \text{ kg/mol}$
Dry density of membrane (Nafion 112), $\rho_{dry}$	$1.98 \times 10^3 \text{ kg/m}^3$

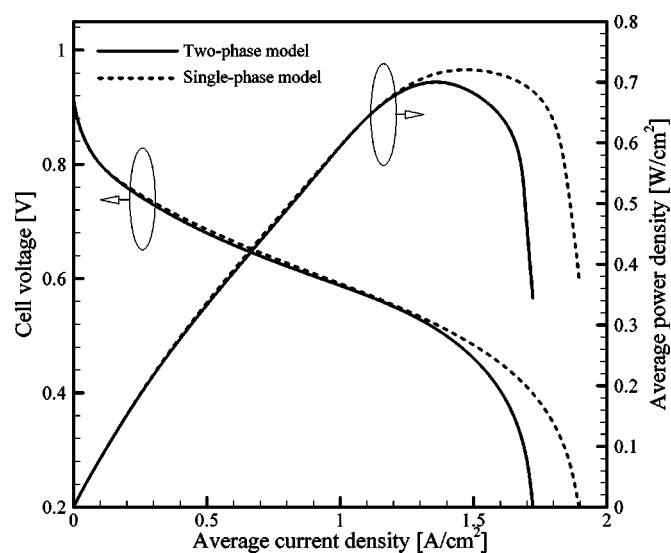
A simple schematic of the grid structure and geometry of the test fuel cell is given in Fig. 1. For these comparison calculations, the cell operating temperature and both inlet temperatures are specified as 80°C, and the inlets are fully humidified at 80°C. Both reactant streams have constant flow rates corresponding to a stoichiometric flow ratio of 2 (*i.e.*,  $\zeta_{ac} = 2$ ) at the reference current density of 1 A/cm<sup>2</sup> and have an inlet pressure of 1.5 atm.

Figure 2 shows the complete steady-state polarization curves predicted by both the two-phase and single-phase models. Both models predict almost the same performance up to an average current density of 1.4 A/cm<sup>2</sup>. Note that in the present calculations, the cell stoichiometry is based on a reference current density (*e.g.*, 1 A/cm<sup>2</sup>), rather than the real current density. Therefore, the gas flow rate is constant at all current densities, which is relatively high in the low current density range, thereby making flooding effect negligible.

However, when the cell is operated at a current density beyond 1.4 A/cm<sup>2</sup>, a significant difference between the two model predictions starts to appear. The two-phase model predicts a lower performance compared to the single-phase model owing to the effects of two-phase transport and flooding in the porous GDL. In the higher cell voltage range (0.5–0.8 V), the cell performance is mainly limited by the ohmic losses in the membrane and catalyst layers, and because the inlet streams are fully humidified, the entire membrane remains almost fully hydrated under all cell voltages, and the proton conductivity thus remains the same for both cases. The water pro-

**Table III. Dimensional parameters of two-channel serpentine PEFC.**

Description	Value
Cell length	70 mm
Cell height	3 mm
Gas channel width/height	1 mm
Gas channel height	1 mm
Anode/cathode GDL thickness	300 $\mu\text{m}$
Anode/cathode catalyst layer thickness	10 $\mu\text{m}$
Membrane thickness (Nafion 112)	50.8 $\mu\text{m}$
Total cell width	2.67 mm



**Figure 2.** Calculated polarization and power curves of two-channel serpentine PEFC at cell temperature of 80°C, inlet pressures of 1.5 atm, fully humidified inlets at 80°C, and anode/cathode stoichiometry: 2 at 1 A/cm<sup>2</sup>.

duction rate is relatively low in this low current density range; hence, the cell does not suffer from severe flooding.

When the average current density is greater than 1.4 A/cm<sup>2</sup> (*i.e.*, the cell voltage is lower than 0.5 V), the cell operates at a mass-transfer limited regime, as signaled by the decline in performance. Here, the single-phase model is capable of predicting the mass-transfer limitations due to depletion of oxygen only; however, the two-phase model also predicts the effect of flooding on the transport of oxygen. In this range, there is a significant amount of water generated due to ORR in the cathode, leading to significant amounts of liquid water forming and severe flooding of the cathode GDL. The polarization curves in Fig. 2 clearly show that the cell performance is lowered by the presence of liquid water. The difference between the average current density predictions of the single-phase model and the two-phase models exceeds 10% for the cell voltage of 0.2 V.

The current density profiles along the flow direction under the two flow channels at the membrane center predicted by both models are given in Fig. 3, in which the effect of flooding is more visible. The current density contours are compared in Fig. 4. Near the channel inlet, the current density predicted by the single-phase model is much higher than that of the two-phase model, as significant flooding of the cathode observed at the same location hampers the current output. Liquid water hinders the oxygen transport and covers a portion of the active catalyst sites, resulting in lower performance near the inlet. In addition, the current distribution predicted from the two-phase model is more uniform because flooding in the upstream regions limits cell performance and consequently oxygen consumption. This leaves more oxygen for downstream regions to produce higher current density. This effect is clearly demonstrated in Fig. 5. Another interesting feature of the current density profiles shown in Fig. 3 is seen around the U-turn location, especially with the single-phase model prediction. Due to the mixing effect and secondary flows around the U-turn of serpentine flow channels, the convective transport of oxygen to the catalyst layer is enhanced; hence, a localized spot of higher performance appears in the single-phase results. A similar phenomenon is also seen in the two-phase results, but at a smaller magnitude, because liquid water existing in the GDL hampers the gas flow and reduces the magnitude of oxygen transport enhancement under very small gas velocities. In the commercial-scale fuel cells, the gas feed velocities through channels would be much higher; consequently, this phenomenon is also expected with a large magnitude even in flooded GDLs.

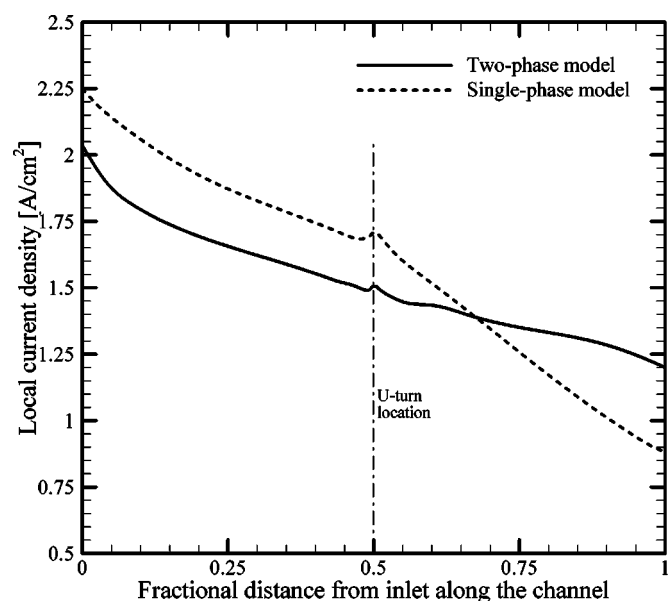


**Figure 3.** Comparison of local current density distributions of two-channel serpentine PEFC at  $V_{\text{cell}} = 0.4$  V.

The most noticeable differences in the two model predictions are observed in the water profiles. In the single-phase model, water vapor does not condense in the GDL; hence, the generated water is easily transported into the gas channel via diffusion and carried downstream by gas convection. Thus, the highest water concentration appears near the middle, as seen in Fig. 6. However, when water is allowed to condense in the two-phase model, liquid water accumulates locally and cannot be carried downstream. Hence, the liquid saturation contour follows the pattern of current distribution, and the highest liquid saturation appears where the highest current density is seen, *i.e.*, near the channel inlet.

It is of interest to analyze the water content of the membrane, because the membrane proton conductivity contributes significantly to the overall cell resistance. In Fig. 7, the water content contours are plotted for the anode side of the membrane. The cathode side of the membrane (not shown here) is overhumidified (*i.e.*,  $a > 3$ ),

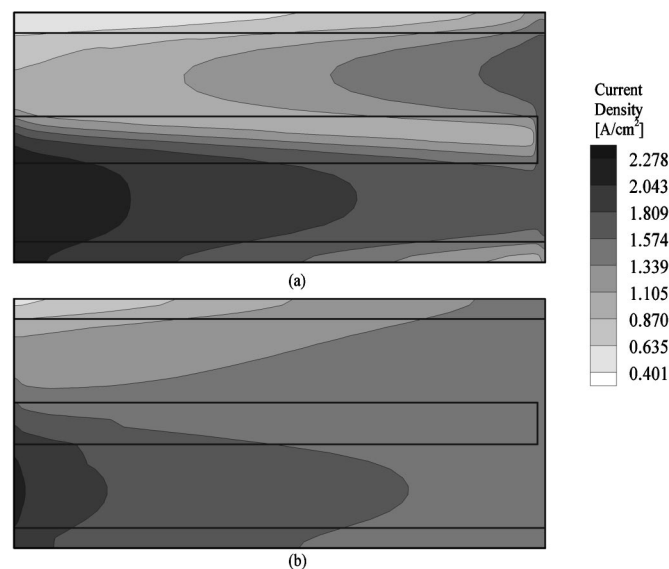


**Figure 4.** Local current density ( $\text{A}/\text{m}^2$ ) contours of two-channel serpentine PEFC at  $V_{\text{cell}} = 0.4$  V: (a) single-phase model and (b) two-phase model.

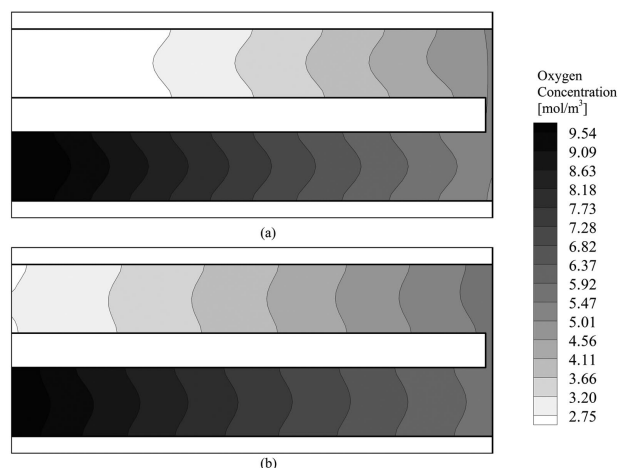


**Figure 5.** Oxygen concentration ( $\text{mol}/\text{m}^3$ ) contours in center of cathode channel of two-channel serpentine PEFC at  $V_{\text{cell}} = 0.4$  V: (a) single-phase model and (b) two-phase model.

because the GDL is already flooded with liquid water. However, the water content at the anode side of the membrane is varying, such that, near the inlet, the anode side water content is lower, suggesting a significant effect of electro-osmotic drag due to higher protonic flux. Near the exit, the current density becomes lower; hence, the amount of water molecules dragged from the anode is lower, resulting in higher water content on the anode side. However, note that in this model the permeation of water across the membrane due to the hydraulic pressure gradient is not accounted for. This additional mode of water transport may affect the water profile in the membrane, particularly in gas-diffusion media with microporous layers (MPLs), in which a much higher hydraulic pressure differential across the membrane due to the finer and more hydrophobic structure of the MPL is observed.<sup>35</sup>

*Effects of operating parameters on two-phase transport and PEFC performance.*—Operating parameters such as humidification and flow rates of inlet reactant streams have a substantial influence on PEFC performance and water transport characteristics. Reactant

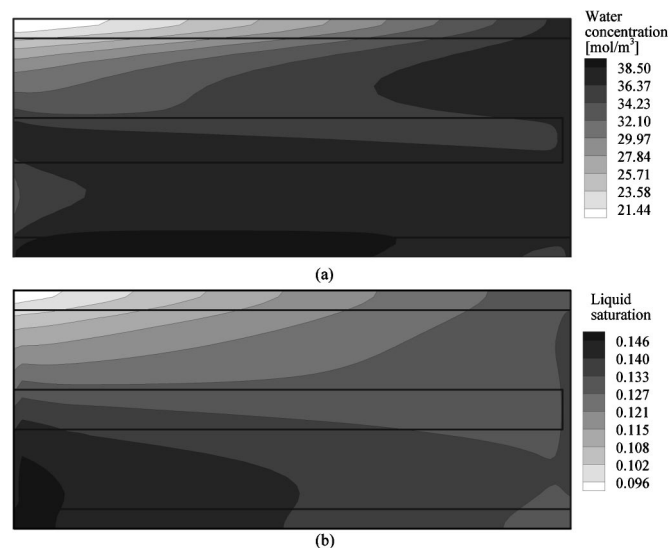


**Figure 6.** Water concentration contours of two-channel serpentine PEFC in cathode GDL-catalyst layer interface at  $V_{\text{cell}} = 0.4$  V: (a) predicted supersaturated water concentration ( $\text{mol}/\text{m}^3$ ) with single-phase model and (b) predicted liquid saturation with two-phase model.

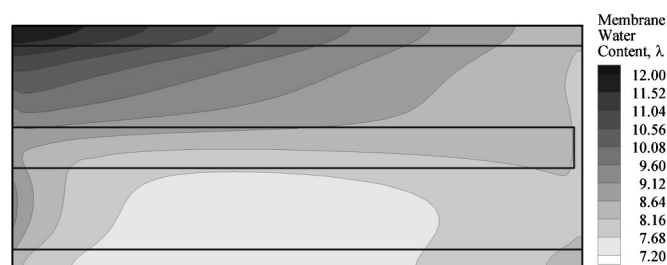


**Figure 7.** Two-phase model predictions of membrane water content  $\lambda$  in two-channel serpentine PEFC at  $V_{\text{cell}} = 0.4$  V at anode catalyst layer-membrane interface.

streams are generally humidified to keep the membrane hydrated and hence minimize the ohmic losses. However, humidification of reactant streams combined with water generation at the cathode leads to condensation of water and severe electrode flooding, lowering the performance, especially at higher current densities and/or lower gas flow rates. In the next subsection, several inlet humidification levels are investigated, and the corresponding transport behaviors are discussed.

**Humidification of inlet streams.**—To investigate the effects of humidification on transport and electrochemical kinetics, a two-dimensional PEFC geometry is considered. The cell dimensions and physical properties of the components are the same as those of the two-channel serpentine geometry described in the previous section and given in Tables II and III. The cell voltage is specified as 0.65 V, and reactant flow rates are prescribed at a stoichiometry of 1.4 for both inlets at the reference current density of 1 A/cm<sup>2</sup>. The relative humidity (RH) of the cathode is varied from 20 to 100% at 80°C, and the anode inlet RH is taken to be 100% except for one of the cases, in which it is 70%. The inlet pressure is 1.5 atm for both inlets.

In Fig. 8, the local current density distributions at 0.65 V for different humidification levels are given at the membrane center along the flow direction. In the fully humidified case, the membrane stays hydrated and the local current density monotonically decreases along the flow direction as a result of mass-transfer limitations due to both oxygen depletion and flooding. For the 70% anode and 20% cathode inlet RH, the membrane stays relatively dry throughout the cell, and shows a membrane ionic resistance-limiting behavior. The current density increases along the flow direction, because the membrane water content is increasing due to water production from ORR. In this case, oxygen depletion is not severe because of the smaller current density. However, for the lower cathode humidity cases with fully humidified anode inlet (*i.e.*, 20% cathode/100% anode and 40% cathode/100% anode), there exists three distinct regimes in the current distribution: (i) the ionic resistance limitation due to the low hydration of the membrane in the first part, (ii) a middle section with highest performance where the membrane is fully humidified, and (iii) mass-transfer limitations due to flooding and/or oxygen depletion in the last part of the cell. As seen from Fig. 9, even with the low cathode inlet relative humidity, *e.g.*, 20% and 40%, the water concentration in the porous GDL exceeds the saturation value, and flooding occurs near the cell outlet. In these cases, the cell suffers from membrane dry-out near the inlet in the anode side, due to the electro-osmotic drag of water to the cathode. Near the inlet, the cathode water concentration is lower; therefore, back-diffusion of water from the cathode to anode does not compensate for the electro-osmotic drag, resulting in the dry-out on the anode side of the membrane.

As shown in Fig. 9, the fully humidified case shows a maximum liquid saturation around 10% near the inlet and decreases in the flow direction due to decreasing water production rate in the cathode catalyst layer. The 10% level of liquid saturation is yielded if using a realistic GDL permeability of the order of  $10^{-12}$  m<sup>2</sup>. Here we

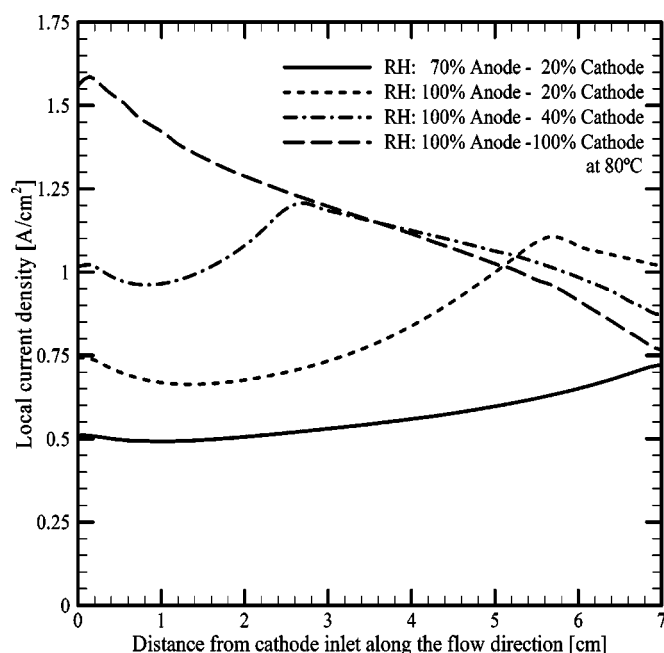


**Figure 8.** Local current density profiles along the channel direction for different humidification levels at  $V_{\text{cell}} = 0.65$  V. Anode and cathode stoichiometries are 1.4 at 1.0 A/cm<sup>2</sup>.

have used  $0.6875 \times 10^{-12}$  m<sup>2</sup> as listed in Table II. Higher liquid saturation values reported in the literature resulted typically from using an unrealistically small permeability value, *i.e.*, 95% maximum liquid saturation with a GDL permeability of  $7.3 \times 10^{-15}$  m<sup>2</sup> in Ref. 19. In comparison, He *et al.* reported a maximum liquid saturation of 3.5% in interdigitated flow-field PEFCs with a GDL permeability of  $10^{-12}$  m<sup>2</sup>.<sup>18</sup>

In the low-humidity cases, product water does not condense until the water vapor concentration in the gas reaches the saturation

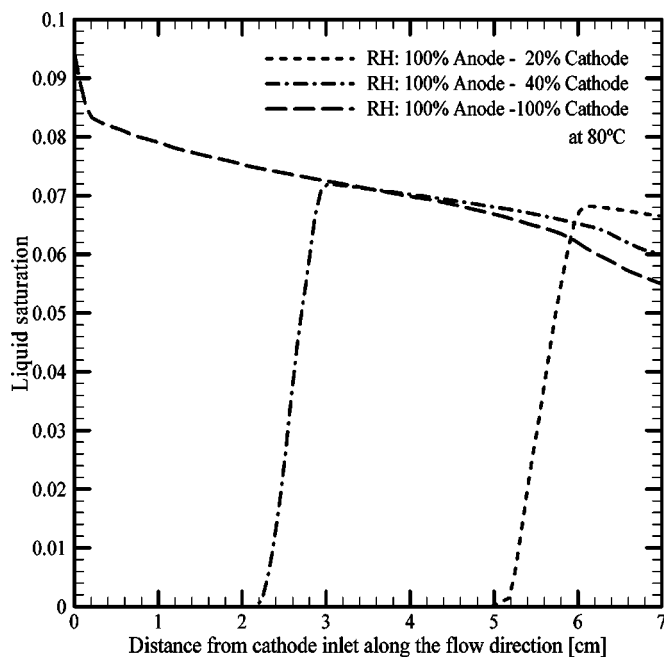


**Figure 9.** Liquid saturation profiles at cathode GDL-catalyst layer interface along the channel direction for different inlet humidification levels at  $V_{\text{cell}} = 0.65$  V. Anode and cathode stoichiometries are 1.4 at 1.0 A/cm<sup>2</sup>.

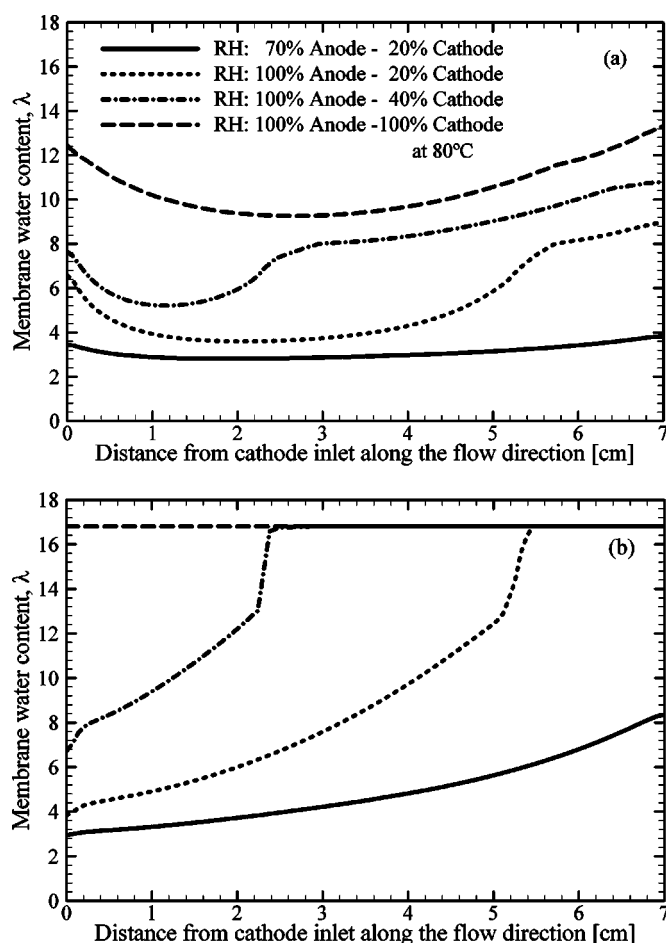


**Figure 10.** Water content of the membrane ( $\lambda$ ) (a) at anode catalyst layer-membrane interface and (b) at cathode catalyst layer-membrane interface, along the channel direction for different inlet humidification levels at  $V_{\text{cell}} = 0.65$  V. Anode and cathode stoichiometries are 1.4 at  $1.0 \text{ A/cm}^2$ .

value; therefore, the condensation front is pushed downstream and its location is directly related to the cathode inlet RH. In the 20% cathode inlet RH case, that the first two-thirds of the cell are free from liquid water, whereas it is predicted that liquid water starts to appear around one-third of the channel length in the 40% cathode humidity case.

Figure 10a and b show the membrane water content profiles on the anode and cathode sides of the membrane along the flow direction, respectively. For all cases, water content on the anode side decreases near the channel inlet and increases toward the outlet, suggesting that the net water flux across the membrane is toward the cathode near the inlet and toward the anode near the outlet. This is attributed to the fact that, due to the lower cathode water concentration near the inlet, the electro-osmotic drag of water from the anode to the cathode is not compensated by the back-diffusion of water. However, near the exit, the water concentration on the cathode side builds up due to water production by ORR, so that back-diffusion from the cathode is enhanced and dominates over the electro-osmotic drag. Thus, the net water flux turns toward the anode. Specific to the fully humidified case (*i.e.*, 100% anode-100% cathode inlet RH), because the current density is also decreasing along the flow direction, the amount of water carried from the anode to the cathode by electro-osmotic drag also decreases. Therefore, the net flux of water from the cathode to the anode increases. In Fig. 10b, it is seen that the water content of the membrane on the cathode side is limited to 16.8, the maximum when the membrane is fully saturated with liquid water at  $80^\circ\text{C}$ . As stated earlier, the membrane water

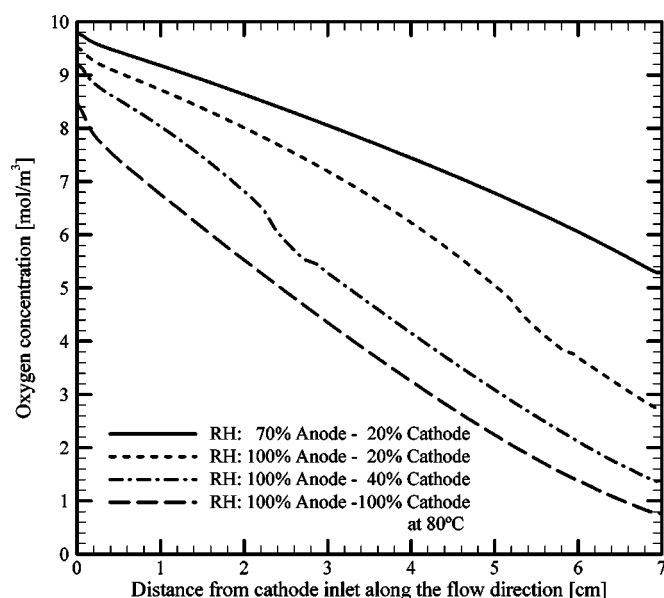


**Figure 11.** Oxygen concentration ( $\text{mol/m}^3$ ) at cathode GDL-catalyst layer interface along the channel direction for different inlet humidification levels at  $V_{\text{cell}} = 0.65$  V. Anode and cathode stoichiometries are 1.4 at  $1.0 \text{ A/cm}^2$ .

content is assumed to be 16.8 once  $a$  exceeds 3 (see Eq. 14).

The oxygen concentration profiles along the flow direction at the cathode GDL-catalyst layer interface are shown in Fig. 11. In the fully humidified case, the local current density profile shows a very similar pattern to the oxygen concentration, indicating that mass transfer is the limiting mechanism for the fully humidified case, as the membrane is kept hydrated everywhere. However, the case with the lowest overall humidification, 70% anode, 20% cathode RH, shows a completely different relation between the oxygen concentration and the current density profiles. The oxygen concentration decreases along the channel due to consumption in the cathode catalyst layer; however, no effect of this depletion is seen on the local current density profile, demonstrating that the cell performance is predominated by the membrane ionic resistance. In low-humidity cases, the oxygen concentration decreases at smaller rates along the channel, where the cathode GDL is free of liquid water, but decreases more sharply at the onset of flooding, where the cell exhibits the highest current density for both of the underhumidified cases; hence oxygen consumption rate is at a maximum. From this point on, the effective diffusivity of oxygen is greatly reduced due to flooding; therefore, the oxygen transport from the channel to the catalyst layer requires a higher concentration gradient, causing a sharper slope in the oxygen concentration profile.

*Flow rate of inlet streams: Stoichiometry.*—In earlier PEFC designs, it was a common practice to use high stoichiometric coefficients to provide abundant reactants to improve performance. However, high stoichiometric coefficients increase the parasitic losses on the air compressor and hence reduce the overall system efficiency. Moreover, higher stoichiometric coefficients adversely affect cell performance by drying out the membrane in low-humidity operation. In this section, we investigate the effect of inlet stoichiometry on the transport characteristics and performance of the PEFC. The same cell geometry as in the previous section is used, the baseline case with 20% cathode, 100% anode relative inlet humidity is selected, and the inlet stoichiometry values for both anode and cathode inlets ( $\zeta_{a,c}$ ) are varied from 1 to 1.4 and to 1.8 at  $1 \text{ A/cm}^2$  reference current density.

In Fig. 12, the polarization ( $I$ - $V$ ) curves for the aforementioned three cases are given. In the very low current density range, because the cell performance is mainly controlled by activation kinetics, all

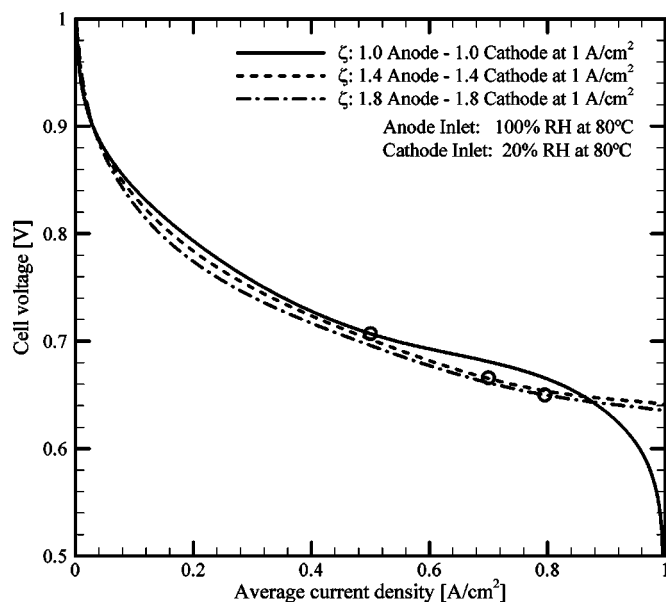


**Figure 12.** Polarization ( $I$ - $V$ ) curves of single-channel PEFC for different stoichiometric ratios at inlet RH: 20% cathode, 100% anode at 80°C.

flow rates yield almost the same performance. In the moderate current density region ( $>0.1$  A/cm<sup>2</sup>), the cell performance starts to differ with different flow rates. The cell performs better when the flow rate is lower, as the water concentration in the channel increases faster, resulting in faster hydration of the membrane. However, in the higher current density range, the lower stoichiometry cell starts to suffer from mass-transfer limitations much earlier than those with the higher stoichiometry, as expected. Furthermore, because the channel water concentration increases faster with lower stoichiometry, the cell experiences liquid water formation earlier. The circles in Fig. 12 indicate the onset points where the cell starts to experience liquid water. When the stoichiometric coefficient is decreased, the PEFC starts to experience flooding effects at lower current densities. In industrial applications, where the reactant stoichiometry is usually defined based on the operating current density rather than a reference value (*i.e.*, stoichiometry-controlled operation), it is expected that flooding may well occur at very low current densities.

In Fig. 13, the local current density distributions along the flow direction are displayed at a cell voltage of 0.65 V. As explained before, the membrane is hydrated much faster at lower flow rates; therefore, the performance peak is seen earlier at lower stoichiometric ratios. However, as the GDL gets saturated with water vapor, water starts to condense, and the cell starts to suffer from flooding of GDL as well as oxygen depletion. The PEFC performance declines due to these mass-transfer limitations. The liquid saturation profiles are given in Fig. 14, showing that with decreasing flow rate, the condensation front moves closer to the channel inlet.

### Conclusions

A multidimensional, two-phase, electrochemistry-transport coupled PEFC model has been developed based on the latest theory of liquid water transport through the hydrophobic GDL. In comparison with the single-phase predictions, two-phase transport phenomena and flooding lowers PEFC performance, due to reduced oxygen transport and active catalytic area. Operating conditions, such as inlet stoichiometry and humidification, are important factors affecting cell performance and two-phase transport characteristics. A detailed analysis of the operating conditions shows that these parameters must be optimized to obtain the maximum available performance.

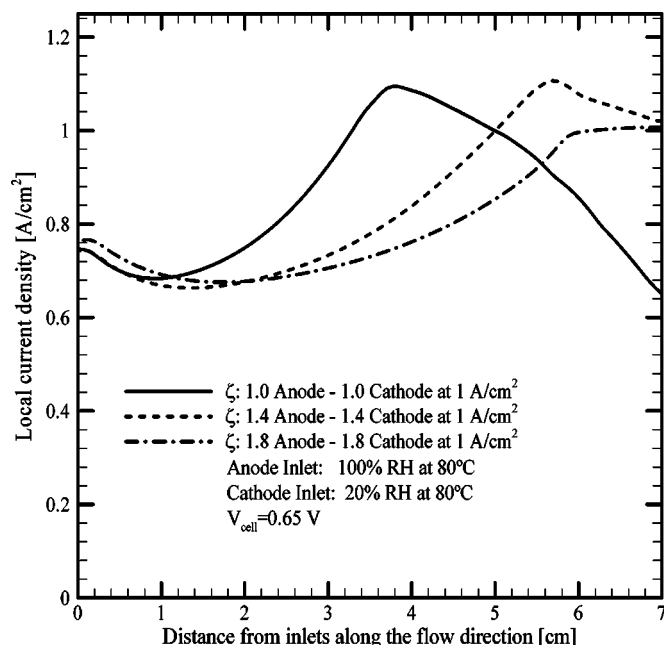


**Figure 13.** Local current density profiles along the channel direction of single-channel PEFC for different stoichiometric ratios at  $V_{\text{cell}} = 0.65$  V at the inlet RH: 20% cathode, 100% anode at 80°C.

In the present model, it is assumed that liquid water in the gas channel exists in very small droplets (*i.e.*, homogeneous two-phase flow) and does not interfere with the gas phase transport; therefore, single-phase transport processes are assumed in gas channels. However, at high current densities where flooding effects are significant, there could be a significant amount of liquid water emerging out of the GDL, forming droplets at the GDL surface. The formation, size, and shape as well as the transport of these droplets are important

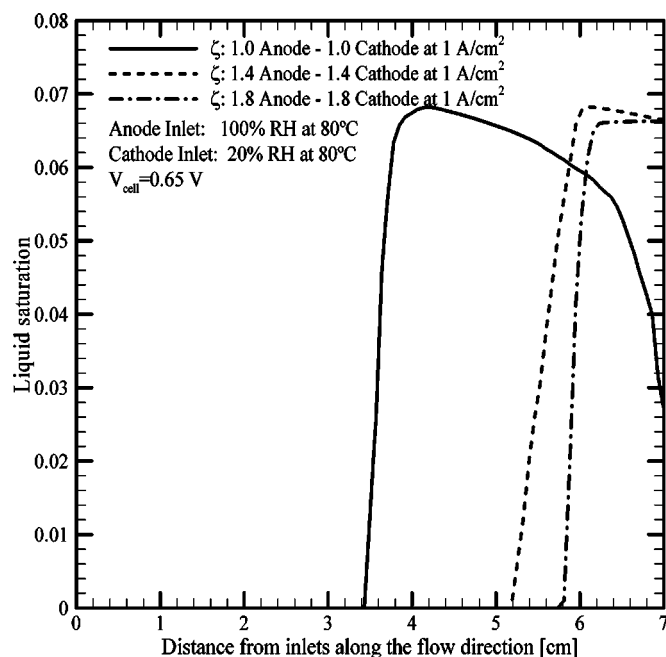


**Figure 14.** Liquid saturation profiles at cathode GDL-catalyst layer interface along the channel direction of single-channel PEFC for different inlet stoichiometric ratios at  $V_{\text{cell}} = 0.65$  V and inlet RH: 20% cathode, 100% anode at 80°C.

processes affecting PEFC operation. Furthermore, the isothermal condition in the PEFC is assumed in the present model, rendering it applicable to single cells with well-controlled temperature. For commercial-size stacks, the MEA temperature could be different by up to 10 K, thereby substantially affecting the water saturation pressure and hence two-phase transport in the GDL. Efforts are presently underway to investigate interactions of temperature variation and two-phase transport in PEFCs by extending the present model.

### Acknowledgments

The funding for this work from the U.S. Department of Energy under cooperative agreement no. DE-FC26-01NT41098, Conoco-Phillips, GM Foundation, and the National Science Foundation under grant no. CTS-9733662 is gratefully acknowledged.

The Pennsylvania State University assisted in meeting the publication costs of this article.

### Appendix

M<sup>2</sup> formulation of species conservation equation in molar concentration

The species conservation equation provided by the M<sup>2</sup> model is written in terms of mass fractions as follows<sup>21</sup>

$$\frac{\partial(\rho m_f^i)}{\partial t} + \nabla \cdot (\gamma_c \rho \mathbf{u} m_f^i) = \nabla \cdot (s D_1^i \nabla \rho m_f^i + (1-s) D_g^i \nabla \rho_g m_f^i) - \nabla \cdot [(m_f^i - m_g^i) \mathbf{j}_i] + S_m^i \quad [\text{A-1}]$$

Note that this equation reduces to the form of a single-phase species transport equation for unity saturations of liquid or gas phase; therefore, it is applicable to all species in all regions of the PEFC. In this equation, the first two terms on the right-hand side account for the liquid and gas phase diffusion, respectively, and the third term is for the capillary transport of liquid water. The last term on the right-hand side denotes a source/sink term on a mass basis arising from electrochemical reactions.

It is assumed that the gases other than water, *i.e.*, oxygen, hydrogen, and nitrogen, are insoluble in the liquid phase; therefore, the mass fraction of water in the liquid phase is unity, whereas those of the other species are zero (*i.e.*,  $m_f^{\text{H}_2\text{O}} = 1$ ,  $m_f^{\text{H}_2, \text{O}_2, \text{N}_2} = 0$ ), thus  $\nabla m_f^i = 0$  for any  $i$ . Consequently, Eq. A-1 reduces to the following

$$\frac{\partial(\rho m_f^i)}{\partial t} + \nabla \cdot (\gamma_c \rho \mathbf{u} m_f^i) = \nabla \cdot [(1-s) D_g^i \nabla \rho_g m_f^i] - \nabla \cdot [(m_f^i - m_g^i) \mathbf{j}_i] + S_m^i \quad [\text{A-2}]$$

In PEFC modeling, expressing the model equations in terms of molar concentrations provides a further advantage: the source and sink terms arising from electrochemical reactions in the preceding equation can be conveniently expressed in molar fluxes. Therefore, converting mass fractions into molar concentrations via

$$\rho m_f^i = C^i M^i \quad [\text{A-3}]$$

and

$$\rho_g m_g^i = C^i M^i \text{ for species other than water} \quad [\text{A-4}]$$

Using Eq. A-4, the species conservation equation (Eq. A-2) can be rewritten in molar concentrations as

$$\frac{\partial(M^i C^i)}{\partial t} + \nabla \cdot (\gamma_c \mathbf{u} M^i C^i) = \nabla \cdot [(1-s) D_g^i \nabla M_g^i C^i] - \nabla \cdot \left[ \left( m_f^i - \frac{M_g^i C^i}{\rho_g} \right) \mathbf{j}_i \right] + S_m^i \quad [\text{A-5}]$$

or

$$\frac{\partial(C^i)}{\partial t} + \nabla \cdot (\gamma_c \mathbf{u} C^i) = \nabla \cdot [(1-s) D_g^i \nabla C_g^i] - \nabla \cdot \left[ \left( \frac{m_f^i}{M^i} - \frac{C_g^i}{\rho_g} \right) \mathbf{j}_i \right] + S^i \quad [\text{A-6}]$$

where  $S^i$  is the molar-based source/sink term arising from electrochemical reactions and valid only in active catalyst layers.

### List of Symbols

$a$  water activity  
 $a i_o$  transfer current density  $\times$  active catalyst area, A/m<sup>3</sup>  
 $C^i$  molar concentration of species  $i$ , mol/m<sup>3</sup>  
 $D^i$  mass diffusivity of species  $i$ , m<sup>2</sup>/s

$EW$  equivalent weight of polymer membrane  
 $F$  Faraday's constant, 96,487 C/mol  
 $g$  gravity, m<sup>2</sup>/s  
 $\mathbf{j}$  mass flux, kg/m<sup>2</sup> s  
 $K$  permeability, m<sup>2</sup>  
 $k_{rk}$  relative permeability of phase  $k$   
 $m_f^i$  mass fraction of species  $i$ , kg/kg  
 $M^i$  molecular weight of species  $i$ , kg/mol  
 $n_d$  electro-osmotic drag coefficient  
 $p$  pressure  
 $p_c$  capillary pressure  
 $R$  universal gas constant, 8.314 J/mol K  
 $s$  liquid saturation  
 $S^i$  source term of governing equation of conservation of species  $i$   
 $T$  temperature, K  
 $\mathbf{u}$  velocity vector, m/s  
 $U_o$  reference open-circuit potential, V

Greek

$\alpha$  transfer coefficient  
 $\gamma_c$  advection correction factor  
 $\eta$  overpotential, V  
 $\epsilon$  porosity  
 $\kappa$  ionic conductivity, S/m  
 $\lambda$  membrane water content  
 $\lambda_k$  relative mobility of phase  $k$   
 $\mu$  dynamic viscosity, Pa s  
 $\nu$  kinematic viscosity, m<sup>2</sup>/s  
 $\theta_c$  contact angle, °  
 $\rho$  density, kg/m<sup>3</sup>  
 $\sigma$  surface tension, N/m

Subscripts

$a$  anode  
 $c$  cathode  
 $cl$  catalyst layer  
 $e$  electrolyte  
 $g$  gas  
 $in$  inlet  
 $l$  liquid  
 $ref$  reference  
 $rxn$  reaction  
 $s$  solid  
 $sat$  saturation

Superscripts

$O_2$  oxygen  
 $H_2O$  water  
 $H_2$  hydrogen  
 $eff$  effective

### References

1. T. F. Fuller and J. Newman, *J. Electrochem. Soc.*, **140**, 1218 (1993).
2. T. A. Zawodzinski, C. Derouin, S. Radzinski, R. J. Sherman, V. T. Smith, T. E. Springer, and S. Gottesfeld, *J. Electrochem. Soc.*, **140**, 1041 (1993).
3. T. A. Zawodzinski, T. E. Springer, J. Davey, R. Jestel, C. Lopez, J. Valerio, and S. Gottesfeld, *J. Electrochem. Soc.*, **140**, 1981 (1993).
4. X. Ren, T. E. Springer, and S. Gottesfeld, *J. Electrochem. Soc.*, **147**, 92 (2000).
5. T. A. Zawodzinski, J. Davey, J. Valerio, and S. Gottesfeld, *Electrochim. Acta*, **40**, 297 (1995).
6. M. L. Perry and T. F. Fuller, *J. Electrochem. Soc.*, **149**, S59 (2002).
7. K. B. Prater, *J. Power Sources*, **51**, 129 (1994).
8. S. Gottesfeld, in *Advances in Electrochemical Science and Engineering*, Vol. 5, R. C. Alkive, H. Gerischer, D. M. Kolb, and C. W. Tobias, Editors, pp. 195-301, John Wiley & Sons, New York (1997).
9. D. M. Bernardi and M. W. Verbrugge, *AIChE J.*, **37**, 1151 (1991).
10. D. M. Bernardi and M. W. Verbrugge, *J. Electrochem. Soc.*, **139**, 2477 (1991).
11. D. M. Bernardi, *J. Electrochem. Soc.*, **137**, 3344 (1990).
12. T. E. Springer, T. A. Zawodzinski, and S. Gottesfeld, *J. Electrochem. Soc.*, **138**, 2334 (1991).
13. T. E. Springer, M. S. Wilson, and S. Gottesfeld, *J. Electrochem. Soc.*, **140**, 3513 (1993).
14. V. Gurau, H. Liu, and S. Kakac, *AIChE J.*, **44**, 2410 (1998).
15. S. Um, C. Y. Wang, and K. S. Chen, *J. Electrochem. Soc.*, **147**, 4485 (2000).
16. C. Y. Wang, W. B. Gu, and B. Y. Liaw, *J. Electrochem. Soc.*, **145**, 3407 (1998).
17. J. J. Baschuk and X. Li, *J. Power Sources*, **86**, 181 (2000).
18. W. He, J. S. Yi, and T. V. Nguyen, *AIChE J.*, **46**, 2053 (2000).
19. D. Natarajan and T. V. Nguyen, *J. Electrochem. Soc.*, **148**, A1324 (2001).
20. Z. H. Wang, C. Y. Wang, and K. S. Chen, *J. Power Sources*, **94**, 40 (2001).
21. C. Y. Wang and P. Cheng, *Adv. Heat Transfer*, **30**, 93 (1997).
22. L. You and H. Liu, *Int. J. Heat Mass Transfer*, **45**, 2277 (2002).
23. S. Mazumder and J. V. Cole, *J. Electrochem. Soc.*, **150**, A1510 (2003).
24. T. Berning and N. Djilali, *J. Electrochem. Soc.*, **150**, A1589 (2003).

25. C. Y. Wang, in *Handbook of Fuel Cells-Fundamentals, Technology and Applications*, Vol. 3, Part 3, W. Lietsich, A. Lamm, and H. A. Gasteiger, Editors, John Wiley & Sons, Chichester (2003).
26. J.-H. Nam and M. Kaviany, *Int. J. Heat Mass Transfer*, **46**, 4595 (2003).
27. U. Pasaogullari and C. Y. Wang, *J. Electrochem. Soc.*, **151**, A399 (2004).
28. D. B. McWhorster and D. K. Sunada, *Water Resour. Res.*, **26**, 399 (1990).
29. R. E. Meredith and C. W. Tobias, in *Advances in Electrochemical Science and Engineering* 2, C. W. Tobias, Editor, Interscience Publishers, New York (1962).
30. S. Um, Ph.D. Thesis, Pennsylvania State University, University Park, PA (2003).
31. S. Motupally, J. A. Becker, and J. W. Weidner, *J. Electrochem. Soc.*, **147**, 3171 (2000).
32. A. Parthasarathy, S. Srinivasan, and A. J. Appleby, *J. Electrochem. Soc.*, **140**, 2178 (1992).
33. S. V. Patankar, *Numerical Heat Transfer and Fluid Flow*, Hemisphere, New York (1980).
34. F. P. Incropera and D. P. Dewitt, *Fundamentals of Heat and Mass Transfer*, p. 849, John Wiley & Sons, New York (1996).
35. U. Pasaogullari and C. Y. Wang, *Electrochim. Acta*, **49**, 4359 (2004).